



Contents lists available at ScienceDirect

## Journal of Wind Engineering &amp; Industrial Aerodynamics

journal homepage: [www.elsevier.com/locate/jweia](http://www.elsevier.com/locate/jweia)

## Aerodynamics of a stay cable with helical fillets - Part I: Stability and load characteristics

H. Christiansen<sup>a,\*</sup>, J.B. Jakobsen<sup>a</sup>, J.H.G. Macdonald<sup>b</sup>, G.L. Larose<sup>c,1</sup>, H.R. Bosch<sup>d</sup><sup>a</sup> Department of Mechanical and Structural Engineering and Material Science, University of Stavanger, Norway<sup>b</sup> Department of Civil Engineering, University of Bristol, UK<sup>c</sup> National Research Council Canada, 1200 Montreal Road, Ottawa, Ontario, Canada<sup>d</sup> Aerodynamics Laboratory, Federal Highway Administration, McLean, Virginia, USA

## ARTICLE INFO

## Keywords:

Bridge stay cable  
Helical fillets  
Inclined circular cylinder  
Cable instability  
Surface pressures  
Sectional loads  
Quasi-steady theory  
Reynolds number

## ABSTRACT

The aerodynamic behaviour of a bridge stay cable with helical fillets in smooth flow at high Reynolds numbers is presented in this paper. The cable response and related sectional load characteristics were studied experimentally on a 1:1 scale cable section model. The studies showed that a cable with helical fillets inclined 60° to the flow could experience large amplitude wind induced vibrations and that the occurrence of vibrations were highly dependent on cable surface irregularities. The ambition is not to explain fully the excitation mechanism, but to present global and local influences of the helical fillets on the flow field. It was revealed that the flow field around the cable shifted between semi-stable transition states which took place when the transition from laminar to turbulent flow propagated from the free shear layers to the boundary layer. The transitions would form locally and spread along the cable axis. The helical fillet appeared to dominate the local flow structures when located at an angular position between 40° and 130° from the stagnation region. In the stagnation and base regions, the surface irregularities appeared to dominate. Furthermore, the helical fillets displaced the mean stagnation line. The application of quasi-steady theory with the measurement data available appeared not to be able to explain the vibrations.

## 1. Introduction

The first application of helical fillets to bridge stay cables were on the Normandy Bridge in France. The purpose of the helical fillets was to mitigate rain-wind induced vibrations (RWIV) which most likely compose 95 % of all inclined bridge cable vibrations according to Gimsing and Georgakis (2012). The efficiency of different fillet designs was examined in precipitation conditions at the Centre Scientifique et Technique du Bâtiment (CSTB) in Nantes by Flamand (1995) before the final design was selected for the bridge. Further wind tunnel tests of cables with helical fillets were undertaken in connection with the construction of the Øresund Bridge by Larose and Smitt (1999). However, the efficiency of helical fillets to also mitigate dry inclined cable vibrations has not been verified. There is no compelling evidence that cables with helical fillets installed on cable stayed bridges have experienced large amplitude vibrations, but dry inclined cable vibrations have been observed on cable stayed bridges with smooth cable surfaces, see e.g. Zuo

and Jones (2010). This has led to concerns regarding the aerodynamics of inclined stay cables with helical fillets, and in order to fill this gap in knowledge, wind tunnel experiments were carried out at the National Research Council Canada (NRC) in 2011. Based on those experiments, this paper examines the aerodynamic stability of a dry inclined bridge cable with helical fillets at high Reynolds numbers in smooth flow and the underlying load characteristics.

Helical fillets (also called ribs in the literature) are widely used on bridges in both Europe and the Americas. However, no guidelines to the geometry of the fillet exist which has led to different designs promoted by the cable manufacturers. Examples of various helical fillet designs in use are presented in Table 1 together with the design that was selected for the present study, estimated to be a good representation of actual designs. The cross-section of helical fillets is normally either rectangular or near-circular, with a slightly larger width than height due to the manufacturing process. Should the cross-section of the helical application be round, it is referred to in the literature as a helical wire. Larger

\* Corresponding author. Now at: Svend Ole Hansen Aps, Sankt Jørgens Allé 5C, 1615 Copenhagen V, Denmark.

E-mail address: [hch@sohansen.dk](mailto:hch@sohansen.dk) (H. Christiansen).

<sup>1</sup> Now at: RWDI, 75 Albert Street, Suite 209, Ottawa, ON, K1P 5E7, Canada.

**Table 1**

Typical helical fillet geometries (all double helix). The elliptical shapes were formed by a semi-circular shape squeezed to the cylinder surface.

Bridge	Cable diameter [mm]	Pitch [mm]	Helix angle [degrees]	Pitch to diameter ratio	Helical fillet [mm]	Cross-section helical fillet
Normandie	170	600	41.7	3.5	1.3 high × 2 wide	rectang.
Øresund	250	550	55.0	2.2	2.1 high × 3.0 wide	rectang.
Charles River	178	610	42.5	3.4	1.5 high × 3.3 wide	rectang.
Generic 1	200	600	46.3	3.0	2.0 dia.	round
Generic 2	160	490	45.7	3.1	4.0 dia.	round
Generic 3	200	620	45.4	3.1	2.0 dia x 4.0 wide	elliptical
Generic 4	200	630	45.0	3.1	2.0 dia x 4.0 wide	elliptical
Present study	162	520	44.5	3.2	2.3 high × 2.4 wide	rectang.

helical protrusions of rectangular cross-section known as helical strakes or fins also exist, but have so far not been installed on bridge cables. With a significant height of 10–12% of the cylinder diameter they suppress vortex-induced vibrations and are found on e.g. marine risers and chimneys. Over the years, numerous studies have been undertaken to investigate the influence of various types of helical applications, concerning parameters as the angular position of the protrusion, the shape of the protrusion, the size relative to the cylinder diameter, the pitch length and the number of helical protrusions. A detailed review of the development of the helical applications can be found in Kleissl (2013).

**2. Experimental setup and measurements**

A short introduction to the experimental setup is given here. For in-depth explanations see Jakobsen et al. (2012) or Larose and D'Auteuil (2014).

**2.1. Wind tunnel and model arrangement**

The tests were conducted in the 3 m × 6.1 m x 12.2 m Propulsion and Icing Wind Tunnel at NRC which is an open-circuit wind tunnel, completely open to the atmospheric conditions, drawing outdoor air, pushing it through the test section and ejecting the flow outdoor. The experiments were performed on a 1:1 scale cable model with a mean diameter of 161.7 mm and a length of 6.7 m, see Fig. 1.

At an inclination of 60°, 6.1 m of the cable was exposed to the flow. The cable section model was composed of a central steel core covered with a high density polyethylene (HDPE) tube obtained from a bridge construction site. The mass per unit exposed length of the cable model was equivalent to 66.7 kg/m. It was determined as the mass of the steel core, the HDPE tube, the instrumentation, the mass of the moving parts of the rig and a third of the mass of the active part of the springs, divided by the length of the model that is actually exposed to the flow. The fillet itself had a rectangular cross-section with sharp edges, 2.3 mm thick and



**Fig. 2.** The side of the cable with the helical fillets normal to the oncoming flow near ring 2 for a cable inclination of 45° and a cable rotation of -25°.

2.4 mm wide and was fixed to the surface of the model with double sided tape. The fillet material was stiff plastic. The helical fillet thickness (width) to outer cable diameter ratio was 0.014 (0.015). The helical fillet was installed as a double parallel helix, as done by the manufacturers, with a pitch of 520 mm and a helix angle of 44.5°. The cable diameter, relative size of the helical fillets and the cable weight were representative of common designs for cables in service. Each end of the cable was supported on four springs allowing the cable to move in two principal orthogonal planes normal to the cable axis; along-wind motion described as heave and across-wind motion described as sway. The model was fixed against torsion by the suspension rig. The model aspect ratio was approximately 38 and the turbulence intensity  $I_u = 0.5\%$ . The largest difference in turbulence intensity along the model span was about 0.1%, i.e. the flow conditions were quite uniform. A more complete description of the flow characteristics in the open-circuit wind tunnel is presented in

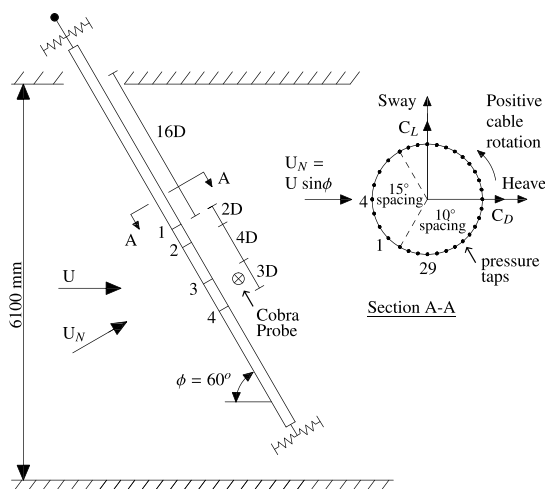


**Fig. 1.** Cable geometry and model setup. Photo taken downwind.

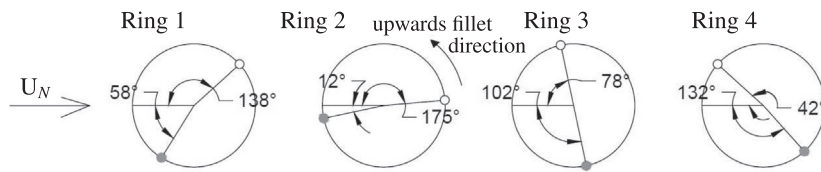


Fig. 3. Location of helical fillets on ring 1-4 at a cable rotation of  $-90^\circ$ . ● fillet normal to the flow, ○ fillet aligned with the flow.

Jakobsen et al. (2012). For reference, experiments were performed on the same cable without the helical fillets, i.e. a smooth cable surface. For the cable with helical fillets, static and dynamic tests were performed, whereas for the smooth cable, only dynamic tests were performed. For the static tests, steel locking pins were inserted at the extremities of the cable model to restrain oscillations.

The test programme involved cable inclination angles towards the flow of  $60^\circ$  and  $45^\circ$ . The former because previous studies have shown the occurrence of the most severe dry inclined cable vibrations for a smooth cable model at this cable inclination angle, see Cheng et al. (2008a,b). Concerning the latter, it is noted that when a cable with helical fillets is inclined to the flow, the helical fillets will induce a geometrical asymmetry. For an inclination of  $45^\circ$  and a helix angle of approximately  $4^\circ$  as in this study, see Table 1, the helical fillet will be perpendicular to the free stream flow on one side of the cable, see Fig. 2. On the other side of the cable, the helical fillet will be aligned with the free stream flow, thereby creating a large asymmetry in the pressure field. Large amplitude vibrations were, however, not recorded for the inclination of  $45^\circ$ , and the results at this angle will thus not be presented in this article. The results can be found in Larose and D'Auteuil (2014).

2.2. Measuring equipment and procedure

To measure the surface pressure distribution, four circumferential rings each consisting of 32 pressure taps were distributed on the model, see Fig. 1. The pressure taps were installed in a previous round of tests which was dedicated to the aerodynamics of a smooth inclined cable where it was not desired to rotate the cable. In those studies the pressure fluctuations near the separation region and the region where fluctuations

of axial flow would have an influence were of interest. The pressure taps were therefore located with smaller angular spacings in those regions. Also, in the stagnation region, the pressure fluctuations are much smaller compared to the separation and base regions. The four rings of pressure taps were besides located with different spacings. The shortest distance of  $2D$  was considered necessary when studying the spatial character (correlation and coherence) of the pressure and force field on the cylinder (see Wootton and Scruton (1970) as also mediated by Dyrbye and Hansen (1999)). The remaining distances were varied and increased, in order to monitor as long a segment of the model as possible. This also provided the data for six different span-wise separations ( $2D, 3D, 4D, 6D, 7D, 9D$ ) as opposed to only three in case of a regular spacing. As described in the present work, the helical fillets represent an additional factor influencing the span-wise organization of the flow field on the cylinder. For a cable rotation of  $-90^\circ$ , the angular positions of the helical fillets are shown in Fig. 3. The helical fillet position at ring 1 is not symmetrical because a pressure tap had to be avoided when the fillet was affixed to the model. The pressure taps were connected to four electronic pressure scanners sampling the signals at a frequency rate of  $312.5\text{ Hz}$ .

Two laser displacement transducers were installed at each end of the cable to measure the sway and heave motion with a frequency rate of  $2500\text{ Hz}$ . Outdoor wind conditions and oncoming flow conditions were recorded in terms of e.g. temperature and humidity. A TFI Cobra Probe, a fast response pressure probe sensing the flow speed fluctuations, was installed upstream of the cable and another in the cable wake to measure the flow fluctuations. The latter was located  $2.5D$  ( $403\text{ mm}$ ) measured horizontally behind ring 3 and  $5\text{ mm}$  inwards of the side of the cable where the helical fillet was nearly normal to the flow. A sampling frequency of  $2500\text{ Hz}$  was used. Each probe monitored the three

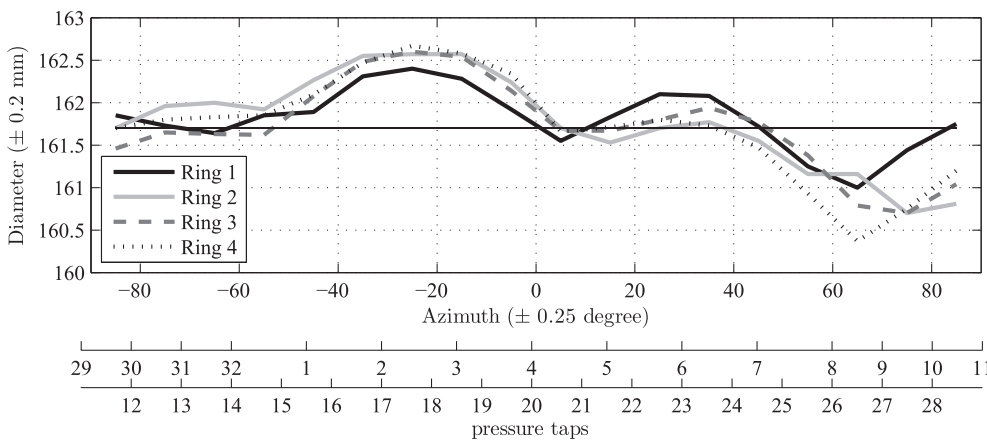
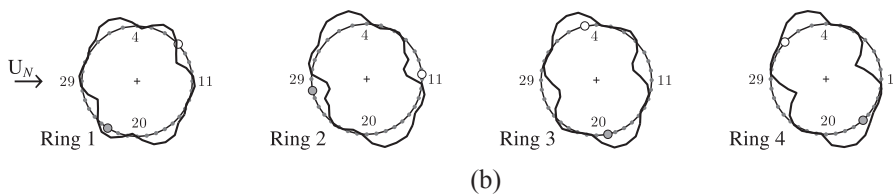


Fig. 4. (a) Variations of the cable model diameter with azimuth at the four pressure tap rings. The nominal diameter of  $161.7\text{ mm}$  is shown. (b) Cable surface deviations shown for a cable rotation of  $-90^\circ$  scaled up by a factor of 50. Based on diameter measurements of the HDPE-tube, the deformations are presented symmetric with respect to a circle for illustration purpose. ● fillet normal to the flow, ○ fillet aligned with the flow.



**Table 2**

Experimental conditions for dynamic experiments of the cable inclined 60° with helical fillets and smooth cable surface, S: sway, H: heave, Sc: Scruton no. Run 122 sustained the most severe vibrations.

Surface	Run no.	Cable rotation [°]	$f_S$ [Hz]	$f_H$ [Hz]	$f_S/f_H$ [-]	$\zeta_{s,S}$ [%]	$\zeta_{s,H}$ [%]	$Sc_S$ [-]	$Sc_H$ [-]
Helix	27, 29, 56, 60, 63, 69, 71, 73, 66, 75	0, -30, -50, -60 -75, 5, 65, 50, -90, -90	1.3885	1.3886	1.000	0.08	0.10	1.6	2.1
Helix	122	-90	1.3886	1.4038	0.989	0.08	0.15	1.6	3.1
Helix	178	-90	1.4038	1.3885	1.011	0.08	0.15	1.7	3.3
Smooth	230, 234, 255	-54.7, 0, -90	1.4038	1.3886	1.011	0.07	0.12	1.5	2.6

components, longitudinal, lateral and vertical of the flow fluctuations.

The data acquisition time was 90 s. The data acquisition process started once a steady-state wind speed and model response were reached. When completed the wind speed was increased to the next set point. Small increments of wind speed were used, generally 1 or 2 m/s depending on the observed behaviour of the cable model. The wind speed sweeps generally covered the entire range of wind speed possible in the facility, from 4 m/s to 36 m/s in 16–18 points. Unless otherwise specified, the wind speed sweeps were carried out with positive increments of wind velocity.

No blockage correction was applied to the force coefficients given the low blockage area ratio of 5 % and because of the uncertainties associated with blockage correction methods for a model inclined to the flow.

### 2.3. Cable surface irregularities

The surface irregularities of an HDPE-tube are composed by i) a systematic shape distortion of the HDPE tube from a circular cylinder and ii) by localised changes in surface roughness. Their influence on the aerodynamic force coefficients has recently been addressed by researchers to be presented in section 3.1. The HDPE surface roughness of the cable model had an average roughness-depth-to-diameter ratio of  $6.5 \cdot 10^{-6}$ , as measured by a mechanical surface-roughness metre. It was measured in connection with a test round carried out in 2008 using the same cable model and test setup, see e.g. Jakobsen et al. (2012). Concerning the shape distortion, a caliper was used to measure the outside diameter of the tube at every 10° of azimuth at the four rings. This revealed that the tube deviated from a circular shape with the deviations being consistent along the cable length, see Fig. 4 (a). The largest difference from peak to valley was approximately 2.3 mm found on ring 4 which is perceptible considering the 2.3 mm fillet thickness. If, for illustration purpose, the deformations relative to the circle are assumed symmetric, representations of the cable model cross-sections are as depicted in Fig. 4(b) although scaled up for visibility. Ring 1 shows some differences from the others but it still displayed the peak and valley indications as the other rings. The consistent spanwise deviations could be due to the extruding process when the tube was manufactured, a condition first suggested by Flamand and Boujard (2009), or the storage of the cable in between tests and its own weight. Deviations of HDPE-tubes on-site can also be introduced during stacking and installation, and through creep due to the cable sag. Throughout the test programme the cable was rotated about its axis (without rotating the springs), see Fig. 1, to determine any effect of the lack of roundness of the model. Through the cable rotation, the helical fillets were in different angular positions relative to the flow at the pressure tap rings. The influence of any misalignment of the helical fillet during installation from a regular helical path will also influence the aerodynamics, but given the size of the helical fillet it was assumed that its simple presence around the cable model would be determinant on the flow field and its influence not so sensitive to small deviations in its path.

### 2.4. Test configurations

Besides changing the axial cable rotation the springs were rotated in their plane as well. This required adjustments of the test setup which

would, together with relaxation of the support springs, cause changes in the natural frequency and the structural damping of the cable. These conditions are listed in Table 2, where the Scruton number is defined as  $Sc = m\zeta_s/\rho D^2$ ,  $m$  being the equivalent mass per unit length of the model,  $\zeta_s$  the structural damping ratio,  $\rho$  the air density and  $D$  the mean diameter of the model.

As seen in Table 2, it was generally desired to have a tuned model or a detuning below 2–3%. As described by Macdonald and Larose (2008b) on real bridge cable stays, frequencies can range from perfect tuning to detuning of about 10% for a pair of modes in orthogonal planes. For rigid supports at both ends of the cable, the even numbered modes are perfectly tuned with each other in pairs (i.e. mode 2 in each plane, mode 4 in each plane, etc.). Odd in-plane modes are affected by the cable sag, but for modes 3 and above the detuning from this effect is negligible. It is only for mode 1 that the sag significantly detunes the in-plane mode from the out-of-plane one, typically by up to about 10 %. Also, since the cable ends are not actually fixed there are slight differences in the natural frequencies due to end motion, which can cause slight detuning. Previous tests (see e.g. Andersen (2010)) had proven that the actual cable model behaviour was not as sensitive to the tuning as otherwise predicted by Macdonald and Larose (2008b).

### 2.5. Repeatability

It is noted in Table 2 that four experimental runs (runs 66, 75, 122 and 178) were carried out for a cable rotation of -90° for the cable with helical fillets, although with some differences in the test parameters. Run 75 was carried out with conditions as close to the original of run 66, to verify the degree of repeatability that could be achieved. In Fig. 5, the amplitudes in sway, which were dominant compared with heave, for the four runs at a -90° cable rotation are depicted (see section 3.1 for an explanation of the modes and the calculation of amplitudes). Vibrations were recorded for each of the four runs at high Reynolds numbers, i.e. at Reynolds numbers above the drag crisis range, in a regime where the along-wind and cross-wind cross-sectional force coefficients did not change significantly with Reynolds number. Concerning the repeatability tests of runs 66 and 75, along with repeatability tests made for other cable model configurations included in Larose and D'Auteuil (2014), the repeatability was seen to be influenced by i) the wind conditions outdoors, in particular outdoor wind fluctuations affecting the turbulence in the test section for wind speeds below 10 m/s ii) the level of structural damping influenced by the interface between the model and the spring suspension system at the lower end of the cable model and iii) the procedure used by the operator to increment the wind speed of the wind tunnel. A thorough description of these conditions and how they were controlled to the extent possible can be found in Larose and D'Auteuil (2014). When all factors were controlled and the dynamic tests were repeated back to back, the variation of the model response with wind speed repeated well. The differences seen between runs 66 and 75, were found to be negligible for the cable model. Run 122 yielded the largest amplitude in sway of 78 mm and was therefore selected as the central element for the analysis of this paper. Run 66, 75 and 178 all resulted in amplitudes nearly half the magnitude of run 122 which could be attributed to differences in the test setup parameters. Also, the vibration phenomenon deals with instability of the boundary layers and cable

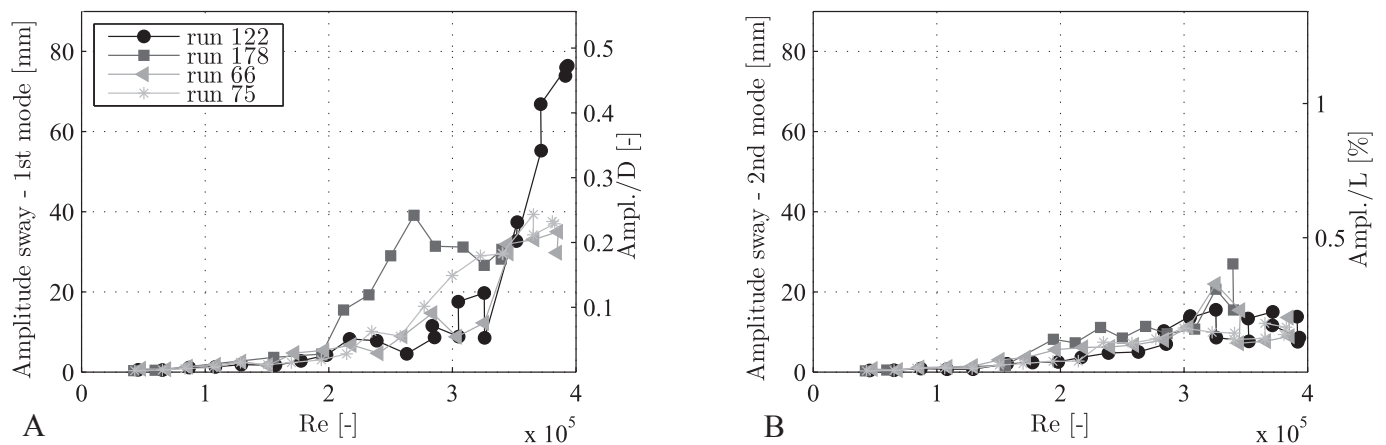


Fig. 5. Amplitude in sway for the cable with helical fillets inclined  $60^\circ$  to the flow at a  $-90^\circ$  cable rotation as a function of Reynolds number, for the varying test parameters listed in Table 2. (a) First mode amplitudes. (b) Second mode amplitudes. L is the entire length of the cable between the supports.

motions which inherently leave room for some randomness in the response.

## 2.6. Applicability and limitations

Given the exploratory nature of the investigation, care was taken to ensure that the experimental conditions were representative to the best of our knowledge of a free-to-respond inclined cable in a uniform flow field. The experiments respected the three main non-dimensional similitude parameters to respect in an aeroelastic experiment: the mass-damping parameter (Scruton number), the Reynolds number and the reduced frequency parameter. The length-to-diameter ratio was maximised while keeping the test section blockage area ratio to under 5%. As previously mentioned, the model was constructed with an HDPE tube obtained from a bridge construction site to ensure that its surface irregularities were representative of field conditions.

The wind tunnel tests presented in this paper were performed in smooth flow as described in section 2.1. Smooth flow is generally considered the worst flow condition in regards to vortex-induced vibrations, galloping-type instabilities and related phenomena. The flow phenomena observed in the experiments are considered representative of what could be observed in the field for open country conditions or open water where the mean wind speed and turbulence level would change only slowly with height and where the dominant turbulence length scales would be much larger than the diameter of the cable. Hereby, the flow fluctuations would be similar to a wind speed modulation slowly varying with time. In general, the flow conditions in the field have characteristics that vary more in space and in time than what was simulated in the current experiments, which are factors that would influence positively the sensitivity of the stay cables to wind induced vibrations. Tests were therefore also performed in a turbulent flow field with a turbulence intensity of 4–5%, which is presented in Christiansen et al. (2015). The results presented in the current paper therefore represent the worst conditions with a focus on better understanding the aerodynamic phenomena at hand.

## 3. Results and discussion

In the following, Reynolds number and the aerodynamic force coefficients are based on the oncoming wind speed  $U$  and the mean cable model diameter  $D$ . The aerodynamic force coefficients are defined as the components normal to the cable axis, and are onwards referred to as the drag and lift coefficients in the along- and across-wind directions respectively, with the orientation shown in Fig. 1.

### 3.1. Aerodynamic stability

The amplitude in sway as a function of Reynolds number for the cable inclined at  $60^\circ$  to the flow is depicted in Fig. 6 for the cable with helical fillets and in Fig. 7 for the smooth cable for various rotations of the cable model about its longitudinal axis. The motion of both cables were dominated by sway motion, and the heave direction is therefore not shown. In sway, the cable had two possible modes of oscillation; the first mode (frequency 1.4 Hz), where both ends of the cable moved in a synchronous manner, and the second mode (frequency 2.1 Hz), where the cable ends oscillated out of phase. A proper representation of the translational modes of the section cable model is the prime target in the design of the model support system. Unintentionally, the spring supports at the two model ends also introduce the “end-to-end” cable model mode. The mode resembles the lowest asymmetric mode in the proximity of the mode “nodes”, but its dynamic properties are normally not tuned to the full-scale counterpart. The quasi-steady analysis presented in section 3.4 addresses the translational modes only. The first mode sway motion was determined by directly averaging the two displacement time-histories recorded at the cable extremities and the second mode sway motion was determined by subtracting the two time-histories one from the other. The amplitudes were obtained by removing the mean from the time-series and averaging the maximum value and numerical minimum value from the first and second mode time-series respectively. The non-dimensional second mode shown in Figs. 6 and 7 corresponds to the rotation about the model span midpoint.

For the cable with helical fillets, two observations can be made from Fig. 6: i) a stay cable at  $60^\circ$  inclination to the flow with a typical helical fillet design can sustain wind induced vibrations in smooth flow, in this case reaching  $0.47D$ , and ii) the amplitudes of the vibrations observed were greatly influenced by the surface irregularities of the HDPE tube as vibrations only occurred at a cable rotation of  $-90^\circ$ . The vibrations were dominated by first mode oscillations. Since the wind speed capacity of the wind tunnel was reached at 39 m/s, it is not possible to say if the large amplitude vibrations would have continued to grow or decay with increasing wind speed. The amplitudes in sway for the smooth cable in Fig. 7 reveal large amplitude vibrations for several of the axial cable rotations tested. For the experimental conditions of this wind-tunnel investigation, the application of the helical fillets therefore reduced the sensitivity of the cable model to dry inclined cable vibrations. The limited-amplitude vibrations for the smooth cable took place in different Reynolds number ranges depending on the axial rotation of the cable and significant vibrations were recorded in both the first and second mode. It is interesting to observe that the first and second mode oscillations did not occur simultaneously, leading to believe that the excitation process

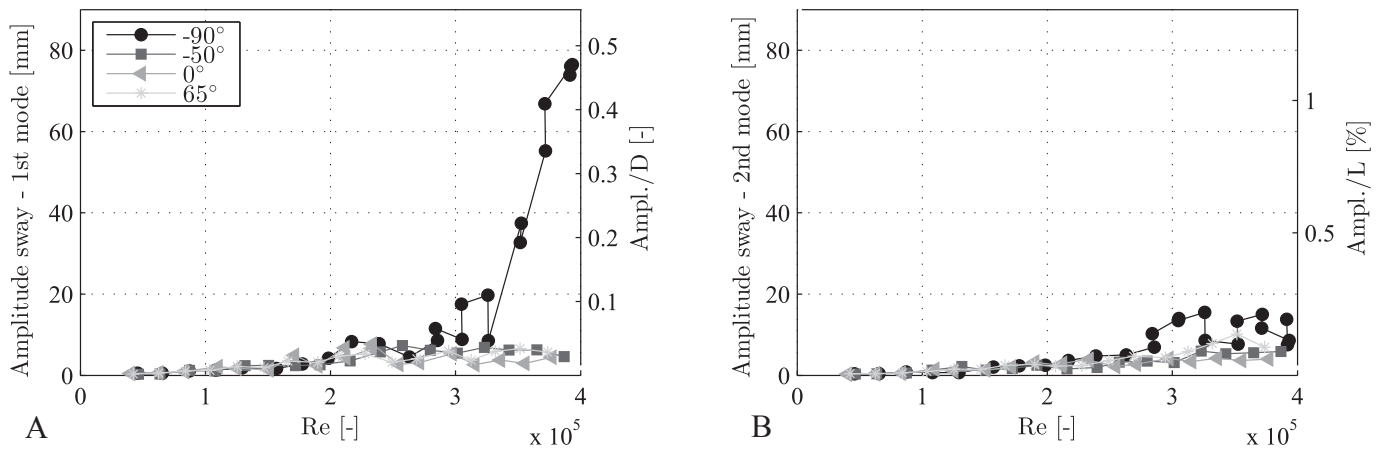


Fig. 6. Amplitude in sway for the cable with helical fillets inclined 60° to the flow at different rotations about the cable axis as a function of Reynolds number. (a) First mode amplitudes. (b) Second mode amplitudes. L is the entire length of the cable between the supports.

has something to do with reduced frequency such as vortex-shedding excitation.

The importance of surface irregularities, i.e. changes in surface roughness or shape distortions on cable aerodynamics, has recently been discovered by researchers. Regarding the changes in surface roughness, it was for example shown by [Matteoni and Georgakis \(2011\)](#) on a nominally smooth cable, that a commercial label with a small width stamped along the length of the cable induced significant changes in the aerodynamic force coefficients when located between the stagnation and separation points. Studies on the dependency of aerodynamic force coefficients on surface irregularities have been undertaken by [Matteoni and Georgakis \(2013\)](#) in dynamic cases and by e.g. [Matteoni and Georgakis \(2012\)](#) and [Benidir et al. \(2015\)](#) in static cases, where the latter however argues that changes in surface roughness have little influence compared to circularity defects. It must also be noted that the surface roughness of a cable in service will change over time due to weather conditions, atmospheric pollution, etc.

The large amplitude vibrations for the cable with helical fillets at a -90° axial rotation shown in [Fig. 6](#), occurred at high Reynolds numbers where the drag and lift coefficients were near constant, see [Fig. 8\(a\)](#). Drag and lift coefficients determined from both the surface pressure tap measurements and the mean displacements at the cable extremities are shown in the figure. Large amplitude vibrations for an inclined cable with helical fillets have also been recorded by [Kleissl \(2013\)](#) at a relative cable-wind angle of 63° for two cable models having  $Sc = 0.58$  and  $0.79$  with different helical fillet designs. The vibrations were limited in

amplitude reaching  $1.4D$  and took place in the critical Reynolds regime, but the initiating mechanisms were not identified. In the studies by [Kleissl](#), the influence of surface irregularities was minimized by sanding the cable surface to isolate the effect of the helical fillets. Large amplitude vibrations of a cable with helical fillets have thus been recorded in two different Reynolds number ranges at different boundary layer transition states; in the critical regime ([Kleissl \(2013\)](#)) and at higher Reynolds numbers where the force coefficients were near constant (the tests at the NRC treated in this paper). Looking at dry inclined vibrations of a smooth cable as a reference case, the vibrations shown in [Fig. 7](#) also took place in different Reynolds number ranges. Similar results were found by [Matteoni and Georgakis \(2013\)](#) who concluded that a smooth cable can experience both limited-amplitude and divergent vibrations depending on the rotation of the cable about its axis, for the case of a cable model with  $Sc = 0.56$  (i.e. three times smaller than the Scruton number in sway for the tests described in this article). Surface irregularities thus can play an important role in the response mechanism. For the current experiments, changes in the test setup may also have affected the response of the cable model as briefly mentioned with respect to [Table 2](#). As discussed in section 2.5, the outdoor wind conditions could also have influenced the behaviour of the cable as the wind tunnel is an open-circuit type. The vibration phenomenon is linked to instabilities of the boundary layers which can be influenced by local flow perturbations combined with model motion. Given that large amplitude vibrations were observed at NRC and by [Kleissl \(2013\)](#) for the total of three different helical fillet designs and for a variety of test conditions, it is expected to

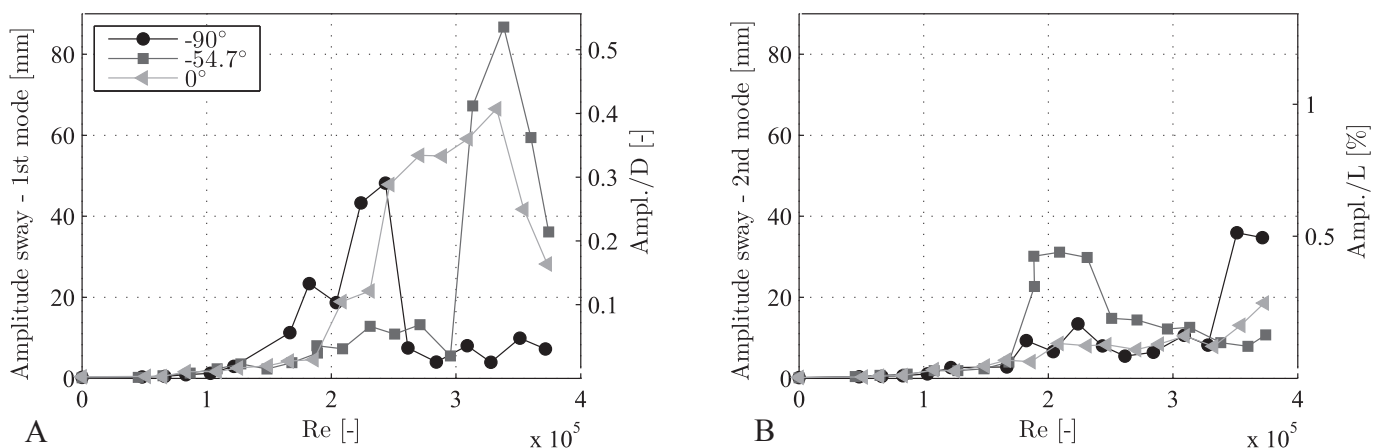


Fig. 7. Amplitude in sway for the smooth cable inclined 60° to the flow at different rotations about the cable axis as a function of Reynolds number. (a) First mode amplitudes. (b) Second mode amplitudes. L is the entire length of the cable between the supports.

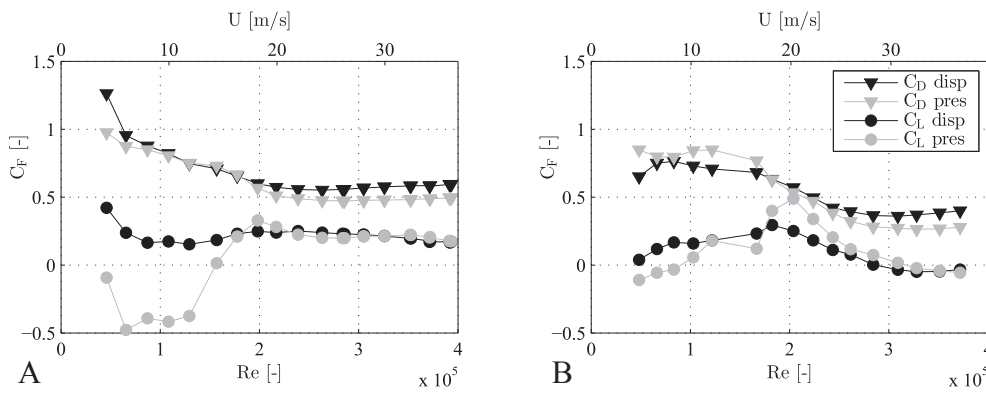


Fig. 8. Force coefficients for a cable rotation of  $-90^\circ$  based on the mean of the surface pressure measurements of the four rings (legend 'pres') and on the displacement measurements (legend 'disp'). (a) Cable with helical fillets. (b) Smooth cable.

be a phenomenon that could occur for most fillet designs in use, at least in wind tunnel tests.

### 3.2. Mean aerodynamic force coefficients

The drag and lift coefficients shown in Fig. 8 are determined from the surface pressure tap measurements and the mean displacements at the cable extremities. The latter serve as an indicator of the expected total load, since the pressure taps show the mean of four discrete sections only. The differences at low Reynolds number could be caused by the resolution of the instruments at these low wind speeds where small displacements occur.

In the high Reynolds number region where the large amplitude oscillations for the cable with helical fillets took place, the lift coefficients as shown in Fig. 8(a) exhibit a non-zero value of approximately 0.2. Inclining a cable with helical fillets will result in an asymmetric geometry as the helical fillets on one cable side will be near normal to the flow, the 'rough' cable side, and on the other side nearly aligned with the flow, the 'smooth' side. The steady lift force is thus generated because the helical fillets cause an asymmetry in separation lines as suggested by Nebres and Batill (1992), directing the lift force towards the smooth cable side. This asymmetry has been confirmed through surface oil visualizations by Kleissl and Georgakis (2012), showing flow patterns on the opposing cable sides that are markedly different. Steady lift coefficients at Reynolds numbers past the drag crisis stand in contrast to a cable normal to the flow, where the lift should cancel out due to periodic variations of the helical fillet on both cable sides. Likewise, for reference, the lift coefficient for a smooth inclined cable is recalled to be zero or near-zero in this Reynolds number range as depicted in Fig. 8(b) and as demonstrated earlier by Larose et al. (2005) and Matteoni and Georgakis (2013) for varying cable inclination angles. Any non-zero values are attributed to surface irregularities.

In the lower Reynolds number range the lift force based on the surface pressure tap measurements is directed towards the rough cable side. The subsequent shift in directions of the lift force taking place for increasing Reynolds numbers, is a behaviour which also has been reported for some inclined stranded cables (depending on the number of outer strands) having similar asymmetric surface characteristics, where the strands on one side are presenting a small angle to the flow, and on the other side are presenting a larger angle to the flow, Macdonald et al. (2008).

A more detailed evaluation of the variations of the aerodynamic force coefficients is given in the following sections.

### 3.3. Local influences of helical fillets

#### 3.3.1. Force coefficients throughout the drag crisis region

The variations of the time-averaged aerodynamic force coefficients with Reynolds number at the four pressure tap rings are depicted in Fig. 9 for the cable with helical fillets. The rate of change of the drag

coefficients from the subcritical range is low with some spanwise variation. At the higher Reynolds numbers a lower drag coefficient value is reached at rings 2 and 4, having the helical fillets in the stagnation and base regions, than at rings 1 and 3 with the helical fillets in the separation region (see Fig. 4(b)). This could indicate that helical fillets located in the stagnation and base regions have a smaller influence on the flow around the cable. Helical fillets located in the separation region could cause a direct separation of the flow, thus widening the wake and increasing the drag. The switch in direction of the lift coefficient for increasing Reynolds number occurs for rings 1, 3 and 4, whereas the lift coefficient remains positive for ring 2 throughout the Reynolds number range covered. Surface pressure distributions will help to study this in the next section. Changes in direction of the lift coefficient as a function of Reynolds number is also observed for the smooth cable shown in Fig. 10.

#### 3.3.2. Mean pressure distributions and instantaneous forces

The mean and RMS surface pressure coefficient distributions at different Reynolds numbers at the four rings are presented for the smooth cable in Fig. 11 as a reference case and in Figs. 13 and 14 for the cable with helical fillets.

It is well known that separation bubbles, also referred to as laminar separation bubbles due to the laminar separation, can form on a circular cylinder normal to the flow during the transition of the boundary layer to turbulent flow. It was also shown, more than 60 years ago, that separation bubbles likewise form on circular cylinders inclined to the flow within a range of inclinations including  $60^\circ$  (Bursnall and Loftin (1951)). A thorough description of pressure distributions for a  $60^\circ$  inclined smooth cable can be found in Jakobsen et al. (2012) so only a short summary is given in the following. The span-wise variation in the pressure distributions seen in Fig. 11(a) has earlier been recorded (Larose et al. (2003)) and is attributed to the inherent three-dimensional flow structure, geometrical imperfections of the cylinder and the model end conditions. The beginning of the drag crisis region therefore varies along the cable. This is shown by the development of a single separation bubble at the Reynolds number of  $1.22 \cdot 10^5$  for ring 1, showing high suction on one side. This is referred to as the TrBL1 regime following the nomenclature presented by Zdravkovich (1997). As the Reynolds number is increased to  $1.82 \cdot 10^5$ , the asymmetric pressure distribution becomes pronounced for the other rings. The separation bubble is not fixed to one side of the cylinder for increasing Reynolds number, but can switch between the sides cf. rings 2-4 in Fig. 10. At  $Re = 2.43 \cdot 10^5$ , a second separation bubble has substantially developed on the opposite cylinder side at rings 1 and 2, i.e. the two-bubble regime TrBL2, whereas at rings 3 and 4 the mean pressure distributions are still more similar to the TrBL1 regime. The presence of the separation bubble is revealed by the "kink" seen for e.g. ring 3 and 4 at  $105^\circ$  clockwise from the stagnation point, but it cannot be seen at all rings because of too large spacings between the pressure taps. The recognition of the separation bubble through the kink in the pressure distribution was first reported by Bursnall and Loftin

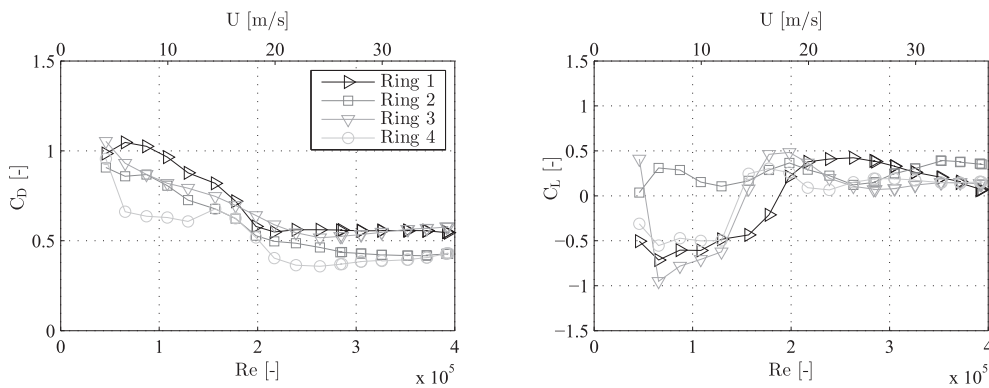


Fig. 9. Force coefficients for the four rings of pressure taps. Cable with helical fillets, cable rotation of  $-90^\circ$ , dynamic case.

(1951). At  $Re = 3.51 \cdot 10^5$ , the bubbles are fully developed on all rings. The kink is not obvious for all rings which could again be due to the pressure tap spacing or because the bubbles have started to disintegrate, thus approaching the supercritical TrBL3 regime.

The pressure fluctuations in terms of the RMS-values shown in Fig. 11(b), in particular for ring 4 at low Reynolds numbers, reveal an important time dependence. Observing the lift time series for ring 4 at  $Re = 1.22 \cdot 10^5$  in Fig. 12(a), asymmetric states are seen which are stable for a period of time and are therefore referred to as semi-stable states. These jumps in states are caused by a single bubble instability with the separation bubble forming alternately on each side of the model. This phenomenon referred to as state jumps was presented by Nikitas et al. (2012) for nominally smooth cables normal to the flow, whereas inclined cables did not show such boundary layer transition instabilities in those studies.

However, the phenomenon was observed by two authors of this paper in 2002, on a static cable inclined  $60^\circ$  to the flow (see e.g. Larose et al. (2003) for test setup) but not reported in publications. Single bubble instabilities have also recently been reported by Benidir et al. (2015) on cable models with helical fillets, inclined  $45^\circ$  and  $60^\circ$  to the flow, and by Demartino et al. (2015) on ice accreted cable models inclined and yawed to the flow. The fluctuations at  $Re = 1.82 \cdot 10^5$  for ring 4 is due to what seems to be random sudden bursts in the lift force between states, see Fig. 12(b), as also reported by Jakobsen et al. (2003) for a smooth cable model inclined  $60^\circ$  to the flow. These single bubble instabilities also took place for the other rings in the drag crisis region but at different Reynolds numbers. Thus, one must be aware that the time-averaged force coefficients do not necessarily represent a stable flow regime but an average over the alternating, unstable flow states. The largest vibrations occurred at  $Re = 2.43 \cdot 10^5$  (see Fig. 7) where state jumps had ceased for all rings but where the second separation bubble was forming (see the time series of the lift coefficient for ring 4 in Fig. 12(c) as an example).

The development of the pressure distributions with Reynolds number for the cable with helical fillets, depicted in Fig. 13, is clearly different at

the two sides of the cable. It is recalled that on a cable inclined to the flow with helical fillets, the helical fillets will on one side of the cable be nearly aligned with the flow, henceforth referred to as the ‘smooth’ side (the upper side in Fig. 13), and nearly normal to the flow on the other side of the cable, referred to as the ‘rough’ side (the lower side in Fig. 13). On the smooth cable side, the fillet does not appear to have a significant influence on the flow field as the boundary layer transition resembles that of a smooth cable, although with some span-wise variations. On the rough cable side, the flow is “controlled” by the fillet, though the influence is reduced in the stagnation and base regions which is to be discussed, and the surface pressure distribution is therefore less dependent on Reynolds number. Furthermore, the smooth cable side may be affected by the helical fillets near normal to the flow. Studies by Ekmekci and Rockwell (2010) have for example shown that a single wire fixed axially along a cylinder normal to flow has global consequences on the flow field.

The rough versus smooth cable side configuration formed by the helical fillets explains the switch in direction of the lift coefficient with increasing Reynolds number seen in Fig. 9 for rings 1, 3 and 4. Generally speaking from tests performed in this test campaign, the influence of the helical fillets seemed reduced at low Reynolds numbers as the direction of the lift force was not consistent with the angular position of the helical fillet near normal to the flow. The negative lift coefficient shown in Fig. 9 at low Reynolds numbers for rings 1, 3 and 4 may thus be due to a combination of the varying influences of surface irregularities and the helical fillets with Reynolds number. It is, however, clear that the sudden shift in the lift coefficients between  $Re = 1.2\text{--}2.0 \cdot 10^5$  is caused by the subsequent propagation of flow transition from laminar to turbulent from the shear layer into the boundary layer on the smooth cable side. The lift force thereafter remains directed towards the smooth cable side.

The angular position of the fillet near normal to the flow affects the local pressure distribution, and the lift coefficient for ring 2 remains, as previously mentioned, directed towards the smooth cable side for all Reynolds numbers tested. Ring 2, having the fillet near normal to the flow in the stagnation region, shows how the flow reattaches to the

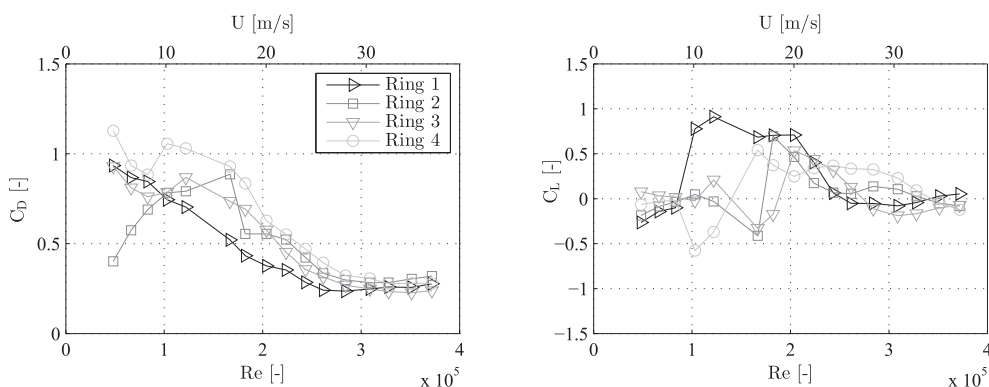


Fig. 10. Force coefficients for the four rings of pressure taps. Smooth cable, cable rotation of  $-90^\circ$ , dynamic case.



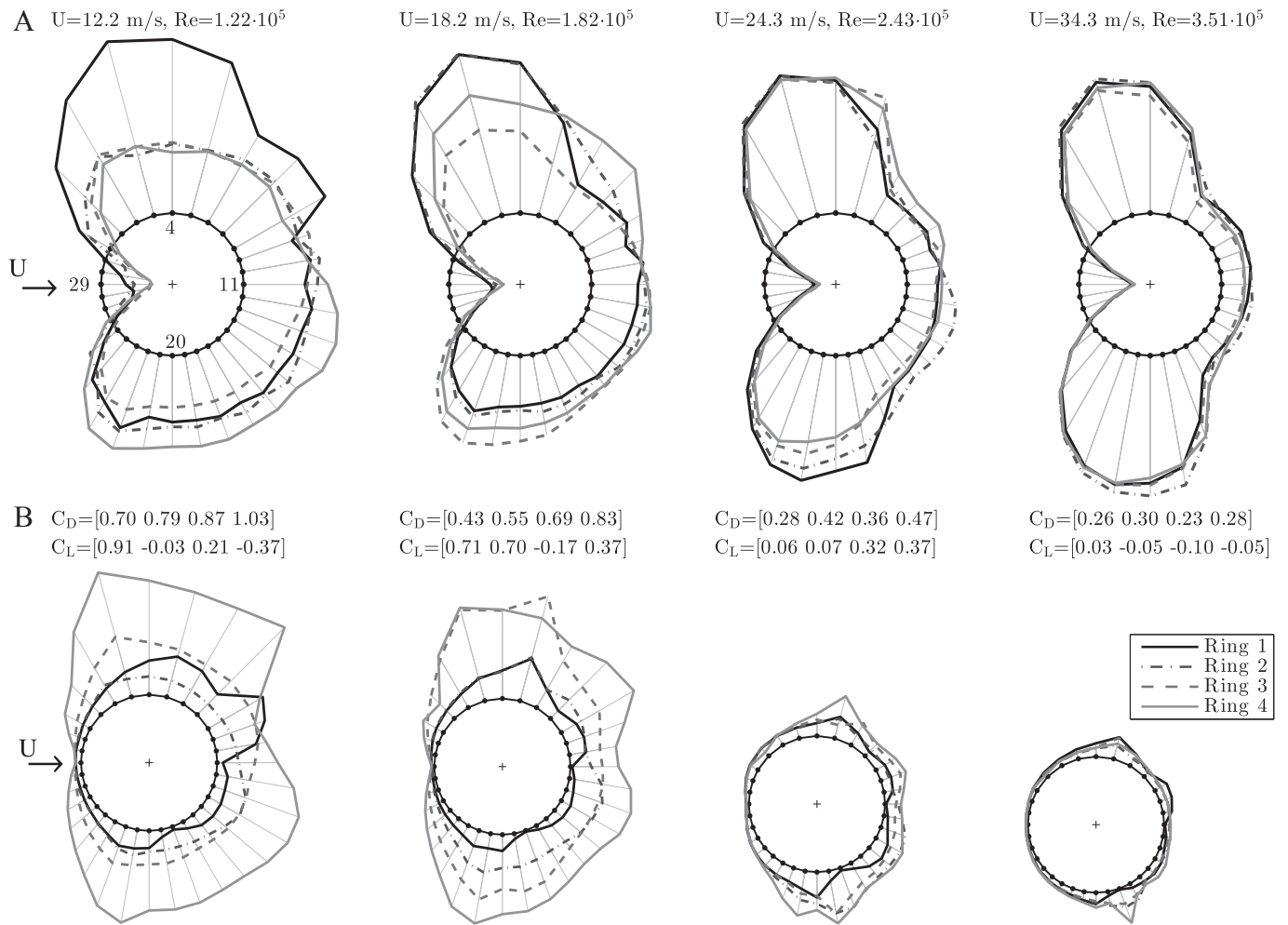


Fig. 11. Smooth cable at  $-90^\circ$  cable rotation, dynamic case. (a) Mean pressure distributions (cable radius corresponds to  $C_p = 1$ ). (b) RMS of pressures (cable radius corresponds to  $C_p = 0.3$ ). Flow coming from the left. Positive lift is directed upwards.

surface after an initial disturbance and has a final separation point at a  $135^\circ$  angular position resembling the separation point seen on the opposite side of the cable. The sudden increase in suction and therefore lift created immediately after the helical fillet at ring 1 and 3 is formed because the fillet trips the flow into an early transition, which leads to an increase in momentum when the flow passes the hindrance - see the high surface pressures RMS-values behind the fillets in Fig. 14. This increase yields a drop in pressure following the fillet, which in turn creates the sudden rise in suction. The tripping-wire effect is to a minor extent seen behind the helical fillet at ring 4.

In Fig. 14, the surface pressure fluctuations observed for ring 3 and 4 are significant at a Reynolds number of  $1.57 \cdot 10^5$  which is in the narrow

Reynolds number region where the mean lift coefficient shifts from a negative to a positive value. A single bubble instability occurs on the smooth cable side, shown for ring 3 in Fig. 15, which creates the same instantaneous jumps in lift force as for the cable without helical fillets. In this case, two semi-stable states exist where the bubble is either present or suppressed. Pressure distributions in Fig. 16 for ring 3 at different time instants illustrate this. The standard deviation in the drag coefficient is higher when the bubble is not present because of an increased flow velocity on the rough cable side (leading to the higher suction) which creates more momentum behind the helical fillet near normal to the flow. For ring 3, only one transition appears during the 90 s sampling period at this Reynolds number, which is shown in Fig. 15. However, they could

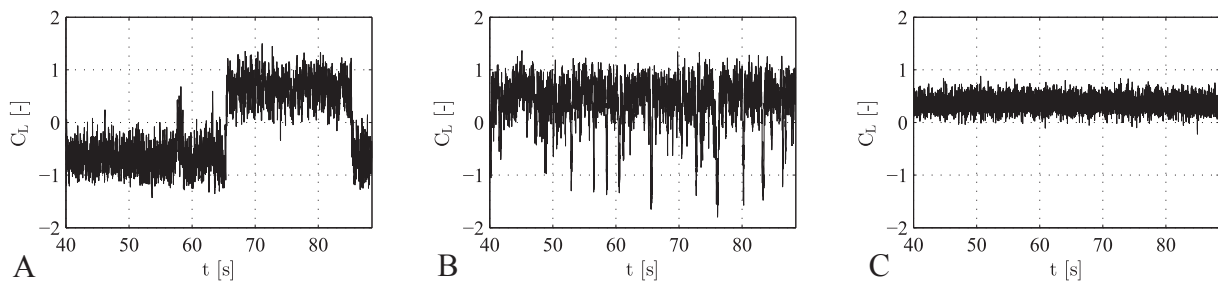
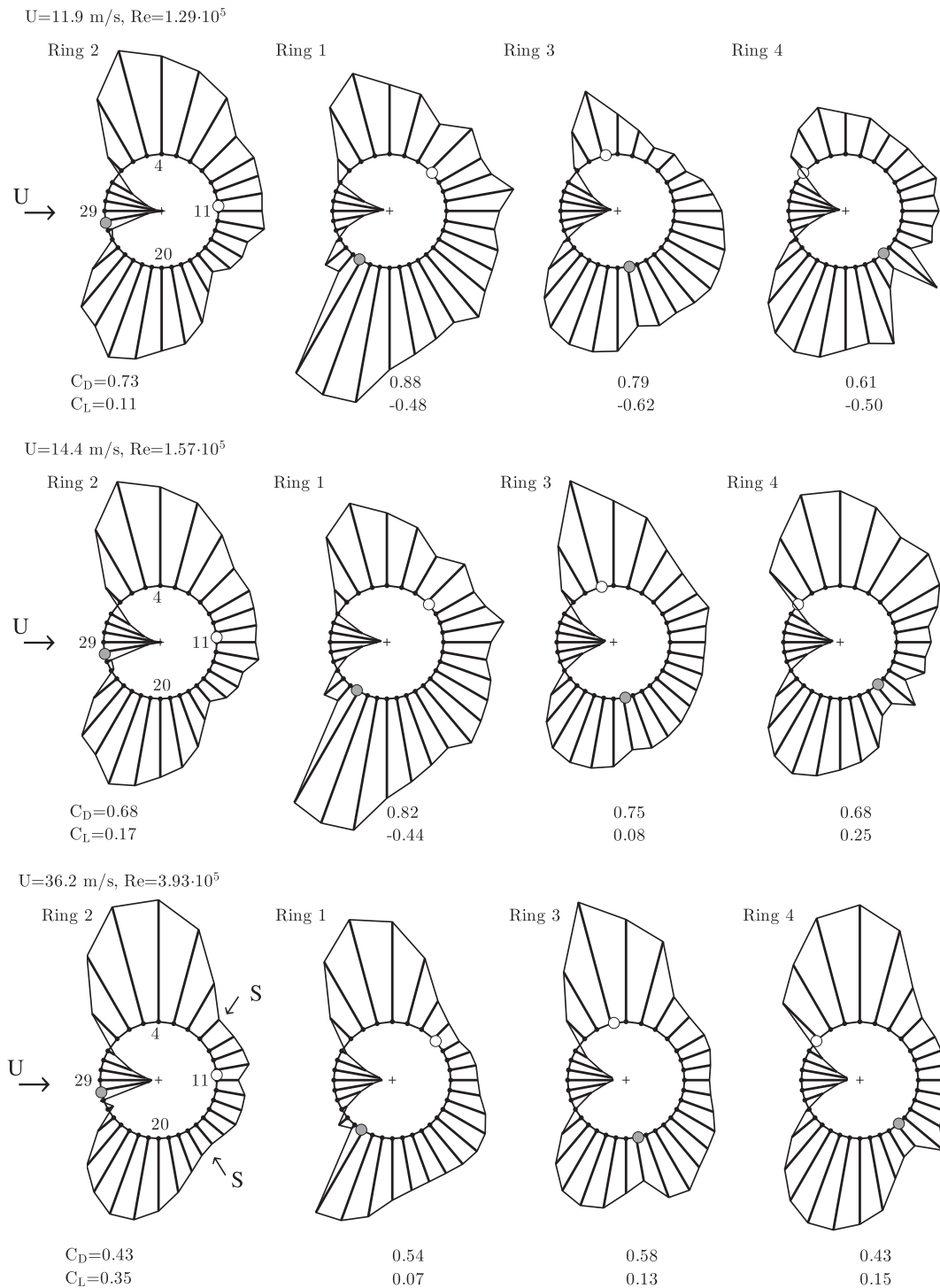


Fig. 12. Time series of lift coefficient  $C_L$  for ring 4, displaying the shift in states. Cable rotation of  $-90^\circ$ , smooth cable. (a)  $Re=1.22 \cdot 10^5$  (b)  $Re=1.82 \cdot 10^5$  (c)  $Re=2.43 \cdot 10^5$ .



**Fig. 13.** Mean pressure distributions for the cable with helical fillets at  $-90^\circ$  cable rotation for the dynamic case. ● fillet normal to the flow, ○ fillet aligned with the flow. To give a better overview of the influence of the angular position of the helical fillets, the rings are shown sequentially for increasing angular position of the helical fillet near normal to the flow (the lower fillet). The cable radius corresponds to  $C_p = 1$ . Positive lift is directed upwards.

appear more frequently, which was observed in other time series, as seen for ring 4 in Fig. 15 as an example. The jumps did not seem to occur at a specific frequency and appeared random in nature, with the semi-stable states lasting nearly an entire sample of 90 s or just one or a few seconds as seen for ring 4 at this Reynolds number. As for the smooth cable model, single bubble instabilities also took place for the other rings in the drag crisis region but at different Reynolds numbers.

The lift coefficient time series for ring 4 is shown in Fig. 15 where there seems to be three possible semi-stable states with a bubble on either

side of the cable or none at all. Note that the helical fillets at ring 4 are located in the stagnation and base regions. One of the state jumps is correlated with the jump for ring 3, but the time instants a, b and c (the same instants as shown for ring 3) show a delay between the rings. This indicates a propagation of the state jump along the cable axis which, in this specific case, has a propagation time of approximately 0.11 s and with a speed of 4.4 m/s ( $U = 14.4$  m/s), see Fig. 17. The idea of the spreading of a transition generated locally on one side of a circular cylinder was first suggested by Schewe (1986) and has, to the authors'

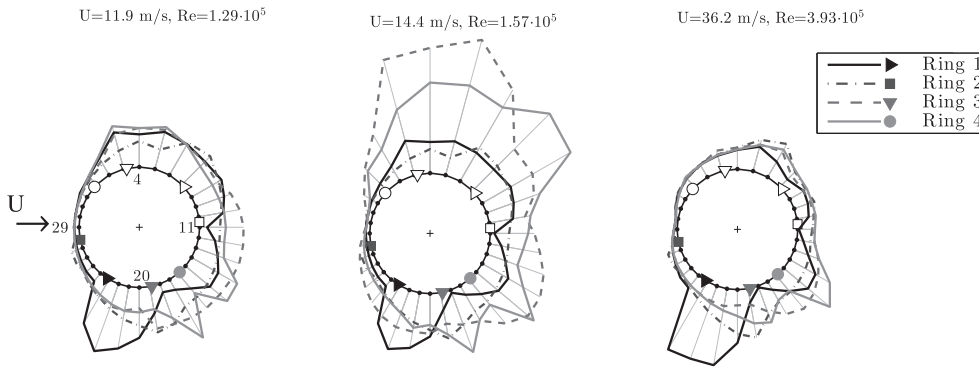


**Fig. 14.** RMS of the surface pressure coefficients for the cable with helical fillets at  $-90^\circ$  cable rotation for the dynamic case, cable radius corresponds to  $C_p = 0.3$ . Flow coming from the left. The markers on the cylinder indicate the positions of the helical fillets of the different rings. Solid: fillet normal to the flow, open: fillet aligned with the flow.

knowledge, not been investigated further. For both the smooth cable and the cable with helical fillets, the propagation would occur between a few of the rings or all of the rings. The transition was in cases also observed at one ring only. It is expected that both surface irregularities and changes in wind characteristics could inhibit the spreading along the cable. It is interesting that the state jump at ring 4 resulted in a lift force directed opposite to that at ring 3, which was not an uncommon observation. In this case, the lift force was, however, after a few seconds “corrected” towards the same direction as ring 3 (Fig. 15) and continued in this state for the remaining data sampling period. This alternate transition between states appears at different Reynolds numbers for the various rings as there is a span-wise variation of the pressures on the cable. Examples of other time series were given by Christiansen et al. (2014) for the various rings and the extent of the semi-stable states with Reynolds number were likewise shown.

Apart from the narrow Reynolds number region where the state jumps occur, the force fluctuations for the cable with helical fillets are seen to be less dependent on Reynolds number compared to the fluctuations of the smooth cable. This is attributed to the ability of the helical fillets to control the flow and therefore disrupt the flow structures otherwise found on a smooth cable. It is also noticed that there is almost no pressure fluctuation at tap 11 and 18 of ring 1 for both cables, which is caused by less responsive pressure taps.

### 3.3.3. Stagnation line

The periodic placement of helical fillets induce periodic variations in the location of the separation lines and the wake width along the cable. The change in position of the separation point for a circular cylinder as a function of the angular position of a single protrusion in a fixed position along the length of a cylinder was presented schematically by Nebres and Batill (1993). Besides affecting the separation lines, helical fillets also affect the location of the stagnation line. It was presented by Kamiya et al. (1979) that the stagnation point on a smooth circular cylinder in the critical Reynolds number range will move towards the shoulder of the cylinder where the separation bubble does not exist. Like separation bubbles, helical fillets introduce asymmetry in the surface pressures

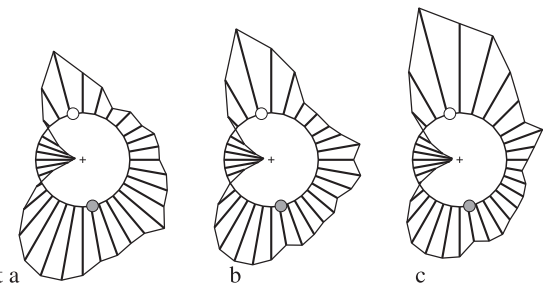


**Fig. 16.** Pressure distributions for ring 3 at  $Re = 1.57 \cdot 10^5$  at the time instants marked in Fig. 15. ● fillet normal to the flow, ○ fillet aligned with the flow.

which displaces the stagnation line periodically. The mean surface pressures from the taps in the stagnation region are depicted in Fig. 18 for ring 1 and 4. The points at the lowest and highest Reynolds numbers,  $1.29 \cdot 10^5$  and  $3.93 \cdot 10^5$ , correspond to the surface pressure coefficient distributions in Fig. 13(a) and (c) respectively.

For a smooth cylinder, the stagnation line would correspond to tap 29 having the highest pressure, and the pressures in tap 28 and 30 would be of equal magnitudes. This is clearly not the case for the cable with helical fillets, where the pressures in tap 29 and 30 are of similar magnitude, indicating that the stagnation line is displaced towards the smooth side of the cylinder. The size of the displacement will depend on the angular positions of the helical fillets. The surface pressures are calculated based on the incoming velocity  $U$  and not the component normal to the cable axis explaining why  $C_p < 1$ .

### 3.3.4. Variations in force coefficients with angular position of helical fillets

Since the helical fillet nearly normal to the flow (the lower fillet on Fig. 13) is to a certain extent governing the flow structure around the cable, the time-averaged force coefficients of the individual rings, with respect to the angular position of that fillet, are presented in Fig. 19 for various cable rotations at three different Reynolds numbers of  $1.3 \cdot 10^5$ ,

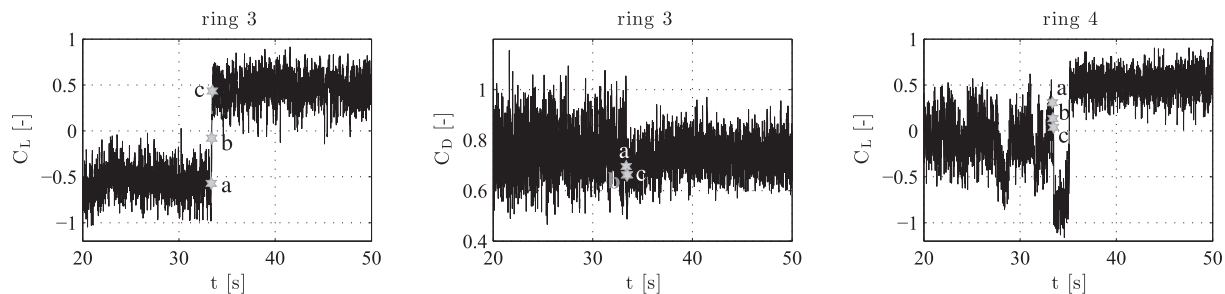


**Fig. 15.** Time series of lift  $C_L$  and drag coefficient  $C_D$  for ring 3 and  $C_L$  for ring 4. Cable rotation of  $-90^\circ$ , at  $Re = 1.57 \cdot 10^5$  displaying a shift in states. Pressure distributions at time instants a, b and c for ring 3 are given in Fig. 16.

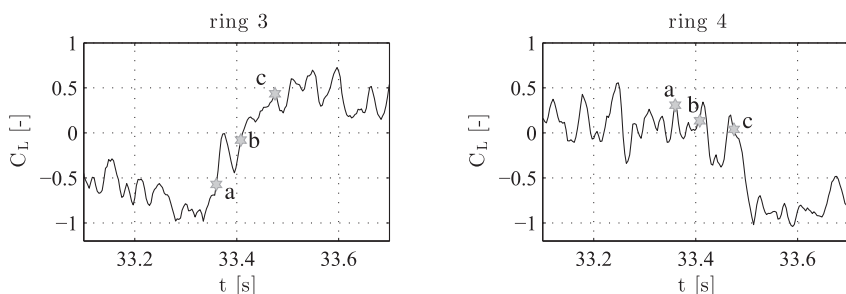


Fig. 17. Time series of lift coefficient  $C_L$  for ring 3 and 4, cable rotation of  $-90^\circ$ , at  $Re = 1.57 \cdot 10^5$  displaying the propagation of the state jump.

$2.0 \cdot 10^5$  and  $3.7 \cdot 10^5$ . The values are shown with four colors, each colour indicating a specific ring. In addition to the colour differentiation, there are different types of markers representing specific cable rotations. For each type of marker there are thus four points representing the angular positions of the helical fillet nearly normal to the flow on each of the four rings for the given cable rotation. As an example the position of the helical fillets for a cable rotation of  $-90^\circ$  are  $58^\circ$ ,  $12^\circ$ ,  $102^\circ$  and  $132^\circ$ , see Fig. 3. These can all be retrieved in Fig. 19 with the marker  $\circ$ , in four different colors. Results from both static and dynamics test are shown and they are generally in good accordance.

Some initial observations can be made. First, the values at low Reynolds number ( $1.3 \cdot 10^5$ ) are scattered, mainly related to the ongoing flow transition on the smooth cable side. As the Reynolds number is increased a more consistent picture is obtained. The presence of a helical fillet near the stagnation point seems to provide at near constant drag force with the angular position, but as the fillet moves towards the separation region it generates a higher drag indicating a widening of the wake. At a helical fillet position of approximately  $80^\circ$ , the drag coefficient starts reducing hence a narrowing of the wake and near a position of approximately  $130^\circ$ , the drag force seems to reestablish itself around the same values as for a helical fillet position near the stagnation point. The mean drag coefficients for a smooth cable with an axial rotation of  $-90^\circ$  are given by the dashed lines in the figure for the average of the surface pressure measurements at the four rings and the mean of the displacement measurements. Given that the magnitudes are nearly similar to the drag for the cable with helical fillets in the stagnation and base regions, the helical fillets do not seem to influence the drag significantly in these regions.

The values of the lift coefficient appear to fluctuate more than the drag coefficient values. At the Reynolds numbers of  $1.3 \cdot 10^5$  and  $2.0 \cdot 10^5$ , the smooth side has not yet undergone complete transition for all rings, which yields the variation in positive and negative lift values. For the Reynolds number of  $3.7 \cdot 10^5$ , a relation between the lift coefficient and the angular position of the fillet can be observed, but values for ring 1 are deviating. This could be caused by the difference in cross section geometry depicted in Fig. 4 or by the lack of symmetry in helical fillet

position shown in Fig. 3 where the helical fillet near normal to the flow was locally displaced and therefore would 'trap' more flow creating a higher momentum behind the helical fillet. To stress this point, the surface pressure coefficient distribution for ring 1 at a  $-90^\circ$  cable rotation is compared with ring 3 at a  $50^\circ$  cable rotation in Fig. 20, where the position of the helical fillet near normal to the flow is  $58^\circ$  and  $62^\circ$  respectively. Model end effects could also contaminate the flow at ring 1, but since it is located at a large distance of approximately 2.5 m or 16D along the length of the cable model from the wind tunnel ceiling this seems less likely. Nikitas et al. (2012) who worked with the same cable model in a previous test phase, concluded that end effects were not significant at the rings by comparing mean pressure profiles for two different end conditions.

The influence of the helical fillet in the vicinity of the stagnation point and the base region was reduced in reference to the drag coefficient, but the non-zero values reached for the lift coefficient in these regions show that the flow is affected by the fillet. Another aspect resulting in a local non-zero lift coefficient is that the pressure tap measurements are performed perpendicular to the cable axis. This cross section is thus made up of several streamlines affected by the periodic placement of the helical fillet and not just by the part of the fillet at the ring section. Surface oil visualisations by Kleissl and Georgakis (2012) for a  $45^\circ$  inclined cable with helical fillets display this well. Furthermore, the lift coefficients in the stagnation and base regions between angular positions of approximately  $0-40^\circ$  and  $130-180^\circ$  (denoted region 1 in Fig. 19) are scattered, which indicates a dependency on surface irregularities. At angular positions between approximately  $40-130^\circ$  (region 2) the influence of the helical fillet appears however to dominate. In this region for  $Re = 3.7 \cdot 10^5$ , ignoring ring 1 due to uncertainties of the deviations from the other rings, the lift coefficient has a value between 0.3 and 0.4 until an approximate helical fillet position of  $100^\circ$ , where it experiences a sudden drop to near 0.1. This development is indicated by black dots in Fig. 19. To describe this transition range, surface pressure coefficient distributions for angular positions of the helical fillet near normal to the flow of  $88.2^\circ$ ,  $102^\circ$  and  $113^\circ$  are shown in Fig. 20. The drop in lift is a

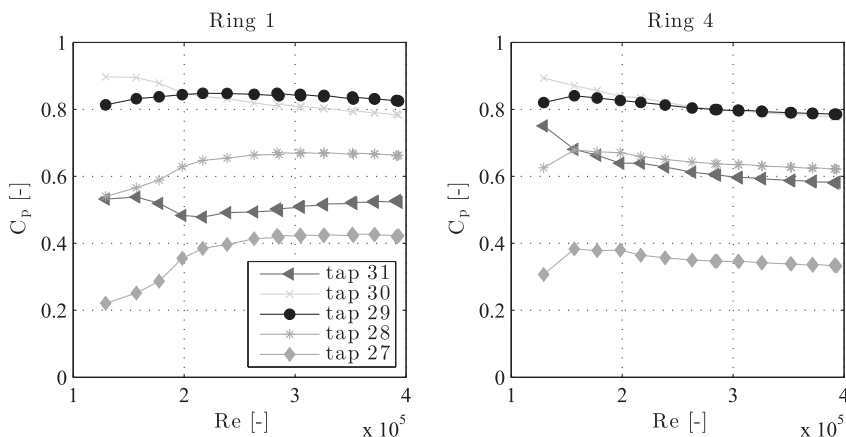
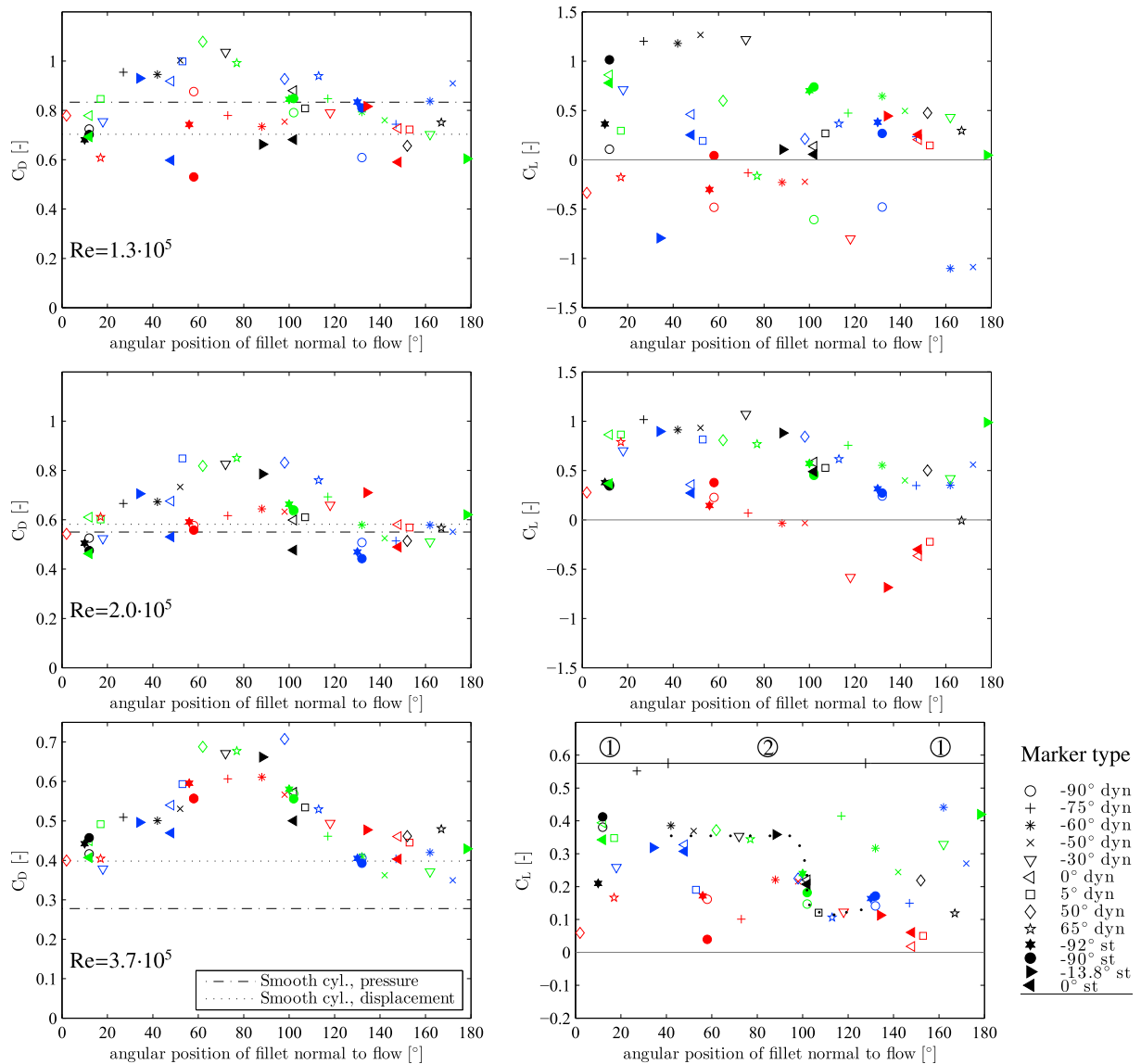


Fig. 18. Mean pressures in taps 27, 28, 29, 30 and 31 in the stagnation region for ring 1 and 4. Tap 29 is located at the point the furthest upstream of the rings. Cable with helical fillets, cable rotation  $-90^\circ$ , dynamic tests.



**Fig. 19.** Local force coefficients with respect to the angular position of the helical fillet nearly normal to flow (the lower fillet in Fig. 13). The stagnation point equals 0°. Both values from dynamic and static tests are shown, the markers indicating different cable rotations. Colors: Red: ring 1, black: ring 2, green: ring 3, blue: ring 4. Dashed lines are the drag coefficients for a smooth cable with an axial rotation of  $-90^\circ$ . Black dots (·) for  $C_L$  at  $Re = 3.7 \cdot 10^5$  indicate the development in region 2.

result of the negative pressure lobe, i.e. the region of suction, in front of the helical fillet near normal to the flow.

Research into flow about circular cylinders with a single protrusion in a fixed position along the cable by Nebres and Batill (1993) has resulted in the division of the flow into four states depending on the angular position of the protrusion. Using perturbations with a circular cross section of varying size  $d/D$  from 0.007 to 0.14 and Reynolds numbers from  $1 \cdot 10^4$  to  $4 \cdot 10^4$ , Nebres and Batill obtained four states, all initiated at different angular positions of the perturbation when changing Reynolds number. State 1: separation bubbles are formed in front of and behind the wire. The boundary layer reattaches and laminar separation occurs. State 2: Separation bubbles are formed in front of and behind the wire, the boundary layer reattaches, transitions to turbulence and delays the final separation. State 3: The front separation bubble forms but the wire leads to complete separation. State 4: The wire is in the base region and the flow is unaffected. A similar division is not obvious for an inclined cable with helical fillets at high Reynolds numbers due to the complex 3D flow field. State 1 resembles what is occurring for ring 2 in Fig. 13, while state 2, which leads to a drop in drag, cannot be identified from the graphs in Fig. 3. The increase and following decrease in drag between an angular

position of  $40\text{--}130^\circ$  is likely due to direct separation of the flow when passing the fillet, i.e. state 3, but the sudden drop in the lift coefficient at an angular fillet position of  $100^\circ$  is a behaviour that differs from the state 3 description. State 4 where the helical fillet is in the base region is also observed. Studies by Ekmekci and Rockwell (2010) at  $Re = 1 \cdot 10^4$  showed that a circular cylinder with a wire with  $d/D = 0.029$  positioned before  $40^\circ$  or after  $120^\circ$  had relatively little influence on the near-wake structure which concurs well with the present findings. Other studies into the influence of a single span-wise surface wire can be found in Ekmekci and Rockwell (2011) and Aydin et al. (2014).

### 3.4. Quasi-steady analysis

Although mean aerodynamic force coefficients do not provide the full picture of the loading on the cable as previously discussed and the vibrations do not concur with the largest changes in the force coefficients with Reynolds number, quasi-steady theory has been used with some success to predict instability regions of smooth cables (Cheng et al. (2008a,b)). In the current section, it is therefore examined whether the large amplitude vibrations of the cable with helical fillets can be

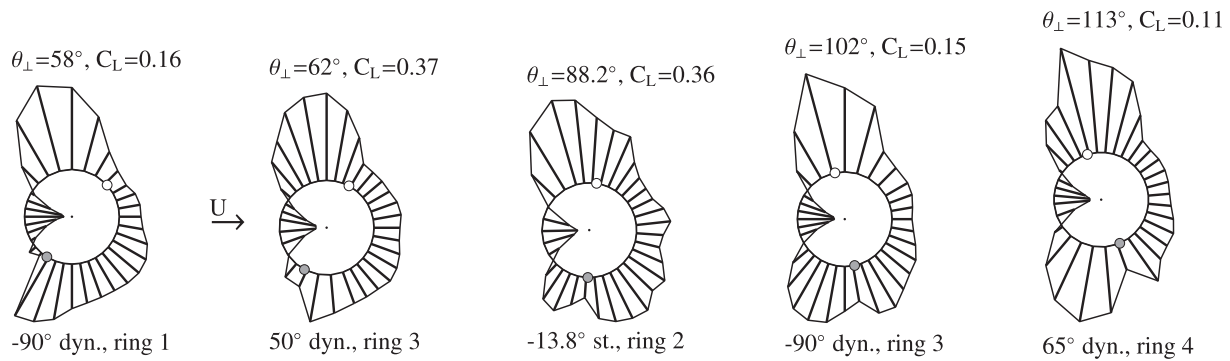


Fig. 20. Mean surface pressure coefficient distributions at  $Re = 3.7 \cdot 10^5$  for different angular positions  $\theta_{\perp}$  of the helical fillet nearly normal to the flow. Based on static and dynamic tests with different axial rotations. ● fillet normal to the flow, ○ fillet aligned with the flow.

explained by quasi-steady theory. If quasi-steady theory is taken to apply for cable vibrations, the instantaneous forces acting on the cable, associated with the instantaneous relative wind velocity, are assumed to be well represented by static force coefficients. Quasi-steady theory seems applicable because of the high reduced velocities in the velocity regime of interest. Having a natural frequency  $f$  of the cable of approximately 1.4 Hz, it is likely that stationary flow conditions can be established as the time period for the flow to pass the cable is much shorter than the vibration period of the cable. With a wind velocity of e.g. 20 m/s a reduced velocity of  $U_{red} = U/fD = 88$  is reached, corresponding to the distance of 88 cable diameters travelled by the mean flow during a single vibration cycle.

Macdonald and Larose (2008a, 2008b) developed an expression for the quasi-steady aerodynamic damping ratio for a cylinder inclined/yawed to the flow in a two degree-of-freedom (2DOF) system, both perfectly tuned and detuned respectively. For the current wind tunnel test setup, the natural frequencies in the sway and heave directions were slightly detuned (Table 2). The expression for a detuned system involves several contributions. From the data available, the contributions related the derivatives of the force coefficients with respect to the cable-wind angle cannot be determined as such measurements were not carried out in the present study. However, it was found that the response trajectories were predominantly across-wind, so these terms are unlikely to be significant and will completely vanish in the case of pure 1DOF across-wind response, see Macdonald and Larose (2006). The remaining contributions are then the change of force coefficients with respect to Reynolds number and with respect to the angle of attack  $\alpha$  equivalent to the cable rotation in this paper. As the cable instabilities occurred in a Reynolds number region where the force coefficients were nearly

constant with Reynolds number ( $3.5 \cdot 10^5 < Re < 4.0 \cdot 10^5$ , see Fig. 8) it is expected that the changes with respect to Reynolds number were not the cause of vibration. A review of galloping models and descriptions of the theoretical background can also be found in Demartino and Ricciardelli (2015) and Nikitas and Macdonald (2014).

The results presented in the following are based on force coefficients determined as the average of the surface pressure measurements at the four rings. The tests were static and the cable was rotated about its axis in intervals of  $2^\circ$ . As the angular position of the fillet alters the load as seen in section 3.3.4, it may however be questioned if a mean value over four discrete sections can represent the forces acting on the cable. The force coefficients could also have been determined by transforming the mean cable end displacements in the dynamic tests, measured by laser displacement transducers, to forces, thus providing a measure of the mean overall wind loading over the entire length of the cable. However, the cable rotation intervals of  $10\text{--}20^\circ$  were too large for a reliable application of the quasi-steady model since the velocity of the cable motion is generally considerably smaller than the wind speed. As an example, for the cable rotation of  $-90^\circ$  at the largest vibration amplitudes where  $Re = 3.93 \cdot 10^5$  ( $U = 36$  m/s), the cable velocity reaches 0.7 m/s. Note that higher turbulence intensity values were observed at low Reynolds numbers, and the aerodynamic damping ratios presented below are therefore for  $Re > 1 \cdot 10^5$ .

The aerodynamic force coefficients as a function of Reynolds number are depicted in Fig. 21 for the various cable rotations. The aerodynamic damping ratio shown in Fig. 22 display instability regions in the drag crisis regions for most of the cable rotations. By studying the contributions involved, the reductions in aerodynamic damping were primarily due to angle of attack dependencies of lift. The change of the lift

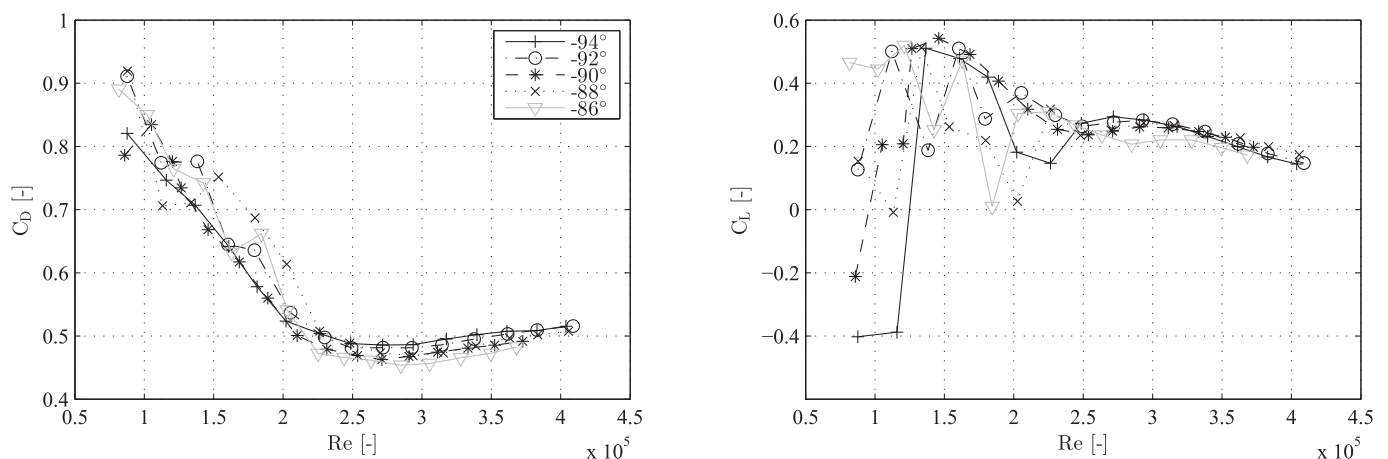


Fig. 21. Drag and lift coefficients for the cable with helical fillets determined as the mean of the surface pressure measurements on the four rings of pressure taps for a series of different cable rotations around  $-90^\circ$ , static tests.

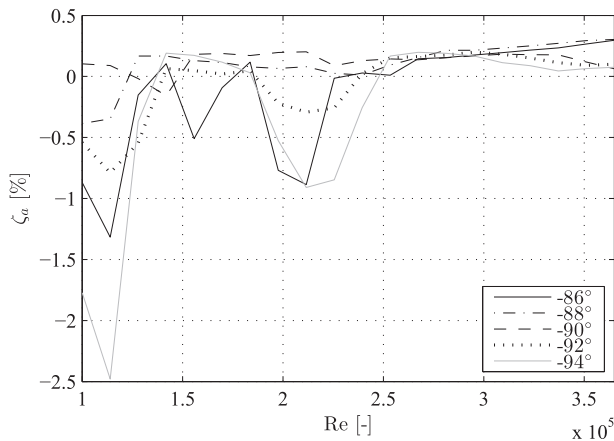


Fig. 22. Aerodynamic damping ratio as a function of Reynolds number for various cable rotations, static tests.

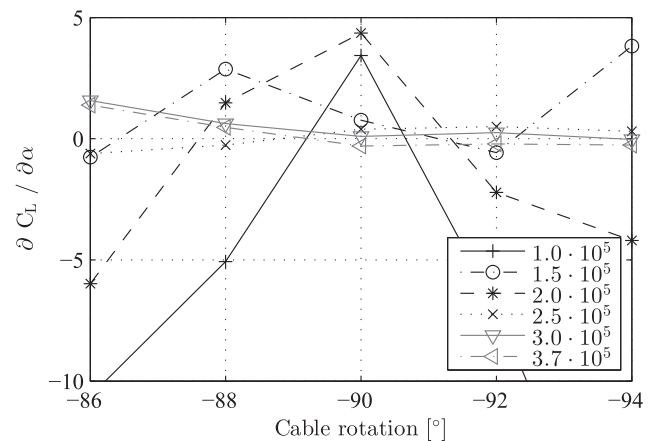
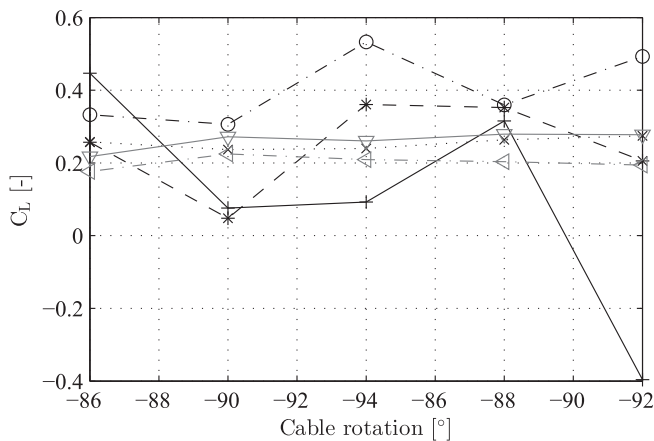


Fig. 23. Mean lift coefficient with respect to the cable rotation (angle of attack)  $\alpha$  at different Reynolds numbers, static tests.

coefficient with the angle of attack is depicted in Fig. 23, where the negative values lead to the instability (the gradients were calculated by using the gradient function in Matlab). As seen in the figure, no significant negative values were obtained for the  $-90^\circ$  cable rotation.

Since quasi-steady theory does not predict instabilities where vibrations occurred, it does not appear to be appropriate to describe the large amplitude motion of the cable with helical fillets. However, this is contradictory with the conclusion drawn in Acampora et al. (2014) where full-scale measurements of the twin cable of the Øresund Bridge were compared with wind tunnel tests. The twin stay cables of the Øresund Bridge have a double helical fillet similar to the fillet of the current study. It is possible that the large amplitude vibrations could be predicted from an evaluation of the aerodynamic forces which in this case is a mean value at four discrete cable sections only. It may be questioned if these sections can represent the total forces acting on the cable. A higher precision in the measurement data in terms of smaller axial cable rotation steps could also be desired, although the aerodynamic force coefficients do not vary significantly at the higher Reynolds numbers where the vibrations were recorded, see Figs. 21 and 23.

#### 4. Conclusion

From the experimental wind tunnel study it was found that a cable with helical fillets inclined  $60^\circ$  to the flow can undergo large amplitude vibrations in dry conditions in smooth flow. The aerodynamic forces acting on the cable and the occurrence of vibrations were highly influenced by surface irregularities of the HDPE-tube as instabilities only were observed at a certain rotation of the cable about its longitudinal axis. The

vibrations took place at high Reynolds numbers where the aerodynamic force coefficients were nearly constant with Reynolds number. Using quasi-steady theory with the data available did not predict instabilities for the cable at the cable rotation and Reynolds number at which they occurred in dynamic tests and did thus not provide an explanation of the vibrations.

The helical fillet nearly aligned with the flow did not have a significant influence on the flow, and the 'smooth' cable side therefore underwent what resembles a classical boundary layer transition. On the opposite 'rough' cable side, the flow was controlled by the helical fillet near normal to the flow, and the local surface pressure distribution was dependent on the angular position of this helical fillet (although remembering that a section normal to the cable axis is affected by several streamlines). The presence of the helical fillets were also found to displace the stagnation line towards the smooth cable side.

In the range of approximately  $40\text{--}130^\circ$ , the helical fillet near normal to the flow seemed decisive regarding the magnitude of the aerodynamic force coefficients, whereas surface irregularities seemed dominating in

the stagnation and base regions,  $0\text{--}40^\circ$  and  $130\text{--}180^\circ$  respectively. This adds to the highly complex three-dimensional flow structure around a cable with helical fillets, where flow regions along the cable alternately shift between helical fillet dominated and surface irregularity dominated.

Large fluctuations in surface pressure coefficients for the cable with and without the helical fillet near the drag crisis region, revealed sudden jumps in the instantaneous lift coefficient for both cable surfaces. This was caused by unsteadiness in the transition of the boundary layer on both cable sides for the smooth cable and on the smooth cable side for the cable with helical fillets, leading to semi-stable transition states. The transitions were found to propagate along the cable axis.

#### References

Acampora, A., Macdonald, J.H.G., Georgakis, C.T., Nikitas, N., 2014. Identification of aeroelastic forces and static drag coefficients of a twin stay bridge cable from full-scale ambient vibration measurements. *J. Wind Eng. Ind. Aerod.* 124, 90–98.

Andersen, T., 2010. Wind Load on Inclined Circular Cylinder in Drag Crisis. Faculty of Science and Technology, University of Stavanger, Stavanger, Norway. PhD Thesis UiS no. 118.

Aydin, T.B., Joshi, A., Ekmecki, A., 2014. Critical effects of a spanwise surface wire on flow past a circular cylinder and the significance of the wire size and Reynolds number. *J. Fluid Struct.* 51, 132–147.

Benidir, A., Flamand, O., Gaillet, L., Dimitriadis, G., 2015. Impact of roughness and circularity-defect on bridge cables stability. *J. Wind Eng. Ind. Aerod.* 137, 1–13.

Burnsall, W.I., Loftin, L.K., 1951. Experimental Investigation of the Pressure Distribution about a Yawed Circular Cylinder in the Critical Reynolds Number Range. NACA Technical Note 2463, Sept.

Cheng, S., Larose, G.L., Savage, M.G., Tanaka, H., Irwin, P.A., 2008a. Experimental study on the wind-induced vibration of a dry inclined cable - Part I: Phenomena. *J. Wind Eng. Ind. Aerod.* 96, 2231–2253.

- Cheng, S., Irwin, P.A., Tanaka, H., 2008b. Experimental study on the wind-induced vibration of a dry inclined cable - Part I: proposed mechanisms. *J. Wind Eng. Ind. Aerod.* 96, 2254–2272.
- Christiansen, H., Larose, G.L., Jakobsen, J.B., Macdonald, J.H.G., Bosch, H., 2015. Comparison of the aerodynamics of bridge cables with a smooth surface and helical fillets in turbulent flow. In: 14th International Conference on Wind Engineering, 21–26 June, Porto Alegre, Brasil.
- Christiansen, H., Jakobsen, J.B., Macdonald, J.H.G., Larose, G.L., Bosch, H., 2014. Sectional load characteristics of a dry inclined helically filleted cable. In: XIII Conference of the Italian Association for Wind Engineering, 22–25 June, Genova, Italy.
- Demartino, C., Ricciardelli, F., 2015. Aerodynamic stability of ice-accreted bridge cables. *J. Fluid Struct.* 52, 81–100.
- Demartino, C., Koss, H.H., Georgakis, C.T., Ricciardelli, F., 2015. Effects of ice accretion on the aerodynamics of bridge cables. *J. Wind Eng. Ind. Aerod.* 138, 98–119.
- Dyrbye, C., Hansen, S.O., 1999. *Wind Loads on Structures*. Wiley.
- Ekmekci, A., Rockwell, D., 2011. Control of flow past a circular cylinder via a spanwise surface wire: effect of the wire scale. *Exp. Fluid* 1–17.
- Ekmekci, A., Rockwell, D., 2010. Effects of a geometrical surface disturbance on flow past a circular cylinder: a large-scale spanwise wire. *J. Fluid Mech.* 665, 120–157.
- Flamand, O., Boujard, O., 2009. A comparison between dry cylinder galloping and rain-wind induced excitation. In: Proceedings of the 5th European and African Conference on Wind Engineering, Florence, Italy, 19th–23rd July.
- Flamand, O., 1995. Rain-wind induced vibration of cables. *J. Wind Eng. Ind. Aerod.* 57 (Issue 2–3), 353–362.
- Gimsing, N.J., Georgakis, C.T., 2012. *Cable supported Bridges - Concept and Design*, third ed. John Wiley & Sons.
- Jakobsen, J.B., Andersen, T.L., Macdonald, J.H.G., Nikitas, N., Larose, G.L., Savage, M.G., McAuliffe, B.R., 2012. Wind-induced response and excitation characteristics of an inclined cable model in the critical Reynolds number range. *J. Wind Eng. Ind. Aerod.* 110, 100–112.
- Jakobsen, J.B., Larose, G.L., Savage, M.G., 2003. Instantaneous wind forces on inclined circular cylinders in critical Reynolds number range. In: 11th Int. Conf. On Wind Engineering, pp. 2165–2173. Lubbock, Texas, June.
- Kamiya, N., Suzuki, S., Nishi, T., 1979. On the aerodynamic force acting on a circular cylinder in the critical range of the Reynolds number. In: AIAA 12th Fluid and Plasma Dynamics Conference, pp. 23–25. Williamsburg, Virginia, July.
- Kleissl, K., Georgakis, C.T., 2012. Comparison of the aerodynamics of bridge cables with helical fillets and a pattern-indented surface. *J. Wind Eng. Ind. Aerod.* 104–106, 166–176.
- Kleissl, K., 2013. *Cable Aerodynamic Control - Wind Tunnel Studies*. Department of Civil Engineering, Technical University of Denmark. Ph.D. Thesis.
- Larose, G., Smitt, L.W., 1999. Rain/wind induced vibrations of parallel stay cables. In: Proceedings of the IABSE Conference, Cable-Stayed Bridges - Past, Present and Future (Malmo, Sweden, June).
- Larose, G.L., Savage, M.G., Jakobsen, J.B., 2003. Wind tunnel experiments on an inclined and yawed circular cylinder in the critical Reynolds number range. In: 11th Int. Conference on Wind Engineering (Lubbock, Texas, June).
- Larose, G.L., Zasso, A., Gippino, S., 2005. Experiments on a yaw stay cable in turbulent flow in the critical Reynolds number. In: 6th International Symposium on Cable Dynamics, pp. 19–22. Charleston, SC, USA.
- Larose, G.L., D'Auteuil, A., 2014. *Wind Tunnel Investigations on an Inclined Stay Cable with a Helical Fillet*. Federal Highway Administration, McLean, VA. Report Number FHWA-HRT-14-070.
- Macdonald, J.H.G., Larose, G.L., 2006. A unified approach to aerodynamic damping and drag/lift instabilities, and its application to dry inclined cable galloping. *J. Fluid Struct.* 22, 229–252.
- Macdonald, J.H.G., Griffiths, P.J., Curry, B.P., 2008. Galloping analysis of stranded electricity conductors in skew winds. *Wind Struct.* 11 (4), 303–321.
- Macdonald, J.H.G., Larose, G.L., 2008a. Two-degree-of-freedom inclined cable galloping - Part 1: general formulation and solution for perfectly tuned system. *J. Wind Eng. Ind. Aerod.* 96, 291–307.
- Macdonald, J.H.G., Larose, G.L., 2008b. Two-degree-of-freedom inclined cable galloping - Part 2: analysis and prevention for arbitrary frequency ratio. *J. Wind Eng. Ind. Aerod.* 96, 308–326.
- Matteoni, G., Georgakis, C.T., 2013. Effects of surface roughness and cross-sectional distortions on the wind-induced response of bridge cables in dry conditions. In: Proc. Of 6th European-african Conference on Wind Engineering, 7th-11th July, Cambridge, England.
- Matteoni, G., Georgakis, C.T., 2012. Effects of bridge cable surface roughness and cross-sectional distortion on aerodynamic force coefficients. *J. Wind Eng. Ind. Aerod.* 104–106, 176–187.
- Matteoni, G., Georgakis, C.T., 2011. Aerodynamic coefficients of dry inclined cables in smooth flow. In: 9th International Symposium on Cable Dynamics (Shanghai, China).
- Nebres, J., Batill, S., 1993. Flow about a circular cylinder with a single large-scale surface perturbation. *Exp. Fluid* 15 (6), 369–379.
- Nebres, J.V., Batill, S.M., 1992. Flow about cylinders with helical surface protrusions. In: 30th AIAA Aerospace Sciences Meeting and Exhibit. Reno, Nevada, paper 92-0540.
- Nikitas, N., Macdonald, J.H.G., 2014. Misconceptions and generalizations of the Den Hartog galloping criterion. *J. Eng. Mech.* 140, 4.
- Nikitas, N., Macdonald, J.H.G., Jakobsen, J.B., Andersen, T.L., 2012. Critical Reynolds number and galloping instabilities: experiments on circular cylinders. *Exp. Fluids* 52, 1295–1306.
- Schewe, G., 1986. Sensitivity of transition phenomena to small perturbations in flow around a circular cylinder. *J. Fluid Mech.* 172, 33–46.
- Wootton, L.R., Scruton, C., 1970. *Aerodynamic stability, seminar on modern design of wind-sensitive structures*. Construction Industry Research and Information Association, CIRIA, London 65–81.
- Zdravkovich, M.M., 1997. *Flow Around Circular Cylinders*, vol. 1. Oxford University Press. Fundamentals.
- Zuo, D., Jones, N.P., 2010. Interpretation of field observations of wind- and rain-wind-induced stay cable vibrations. *J. Wind Eng. Ind. Aerod.* 98, 73–87.